Feature Concatenation based Multilayered Sparse Tensor for Debond Detection Optical Thermography

Junaid Ahmed[1], Abdul Baseer[2], Guiyun Tian[3], Gulsher Baloch[4], Ahmed Ali Shah[5]

Electrical Engineering Department, Sukkur IBA University, Sukkur, 65200, Sindh, Pakistan[1, 2, 4, 5]
School of Automation Engineering, University of Electronic Science and Technology, Chengdu, Sichuan, China[3]

Abstract—Composites being the key ingredients of the manufacturing in the aerospace, aircraft, civil and related industries, it is quite important to check its quality and health during its manufacture or in service. The most commonly found problem in the CFRPs is debonding. As debonds are subsurface defects, the general methods are not quite effective and require destructive tests. The Optical Pulse Thermography (OPT) is a quite promising technology that is being used for detecting the debonds. However, the thermographic time sequences from the OPT system have a lot of noise and normally the defects information is not clear. For solving this problem, an improved tensor nuclear norm (I-TNN) decomposition is proposed in the concatenated feature space with multilayer tensor decomposition. The proposed algorithm utilizes the frontal slice of the tensor to define the TNN and the core singular matrix is further decomposed to utilize the information in the third mode of the tensor. The concatenation helps embed the low-rank and sparse data jointly for weak defect extraction. To show the efficacy and robustness of the algorithm experiments are conducted and comparisons are presented with other algorithms.

Keywords—Improved tensor nuclear norm; low-rank decomposition; concatenated feature space; optical thermography

I. INTRODUCTION

For the task of extracting weak defect information in the thermal sequences of carbon fiber reinforced polymer (CFRP) debonds using the optical pulse thermography (OPT) based technology, post-image processing techniques are generally used. In [1], principal component analysis (PCA) is used along with the OPT for detecting the debonds in the CFRP. The PCA algorithms decompose the thermal sequence data into a low dimensional space using either the eigenvalue decomposition or the singular value decomposition (SVD). The algorithm provides reasonable results for detecting the debond defects in the CFRPs. In [2], another decomposition-based algorithm is proposed called the independent component analysis(ICA). The algorithm is similar to the PCA and provides reasonable results for detecting the debonds in CFRPs. In [3], the authors propose a polynomial-based decomposition algorithm called the thermal signal reconstruction (TSR). It works in the logarithmic domain and performs the polynomial fitting to extract the defect information in the thermal video sequences. The algorithm performs a little better than PCA and ICA however, it has a long-running time. In [4], [5], pulse phase thermography (PPT) is proposed. It employs an extension to the TSR algorithm in the frequency domain and extracts the amplitude and phase information for defect analysis. The PPT algorithm utilizes the Fourier Transform for extracting the

defects information in the thermal sequences. In [6], [7], sparse principal component thermography (SPCT) is proposed for debonding detection in composites. This algorithm is an extension of the PCA algorithm. It induces sparsity into the algorithm. This algorithm works well for the flat shape specimen. In [8], feature embedding is proposed which uses the joint feature space for low-rank and sparse analysis. In [9], a tensor decomposition algorithm is proposed called the ensemble variational Bayes tensor factorization (EVBTF). It employs a multilayer architecture with tensor decomposition. The algorithm is used for detecting the debonds in the CFPR specimen using optical pulse thermography. The specimen under test was the flat rectangular shape CFRPs with debond defects at multiple depths and with multiple diameters. Another multilayer decomposition approach is proposed in [10] called a sparse mixture of Gaussian (S-MoG) for debond detection in composites. The algorithm provides reasonable results for the flat shape CFRP. Also, this algorithm is tested for the irregular shape CFRP V-shaped having debond defects at the elbow location.

The problem with existing approaches and algorithm is that as the depth of the defect on the specimen increases or the diameter of the defect on the specimen decreases, the detection performance gets worse and the algorithms fail to detect the defects. Also, when the existing algorithms were tested on an irregular (V-Shape) specimen their performance is not good [10]. The time consumption that is the running time of the algorithms representing their computational efficiency is another problem that needs to be dealt with for meeting the requirements of the online NDT.

In this paper, we solve the task of debonding detection in CFRP composites using optical thermography by using the concatenated feature space where the sparse data, low-rank data, and reconstructed data are used in a joint concatenated matrix. Further, the eigendecomposition is used to represent this joint feature space. It helps embed the sparse and low-rank data in single feature space for optimization. Further, this is solved by an improved tensor nuclear norm (I-TNN) based core singular matrix utilization tensor decomposition framework. This utilization allows exploiting the tensor data in its third mode which is not fully utilized [11] and helps decrease the computational cost of the overall algorithm due to faster convergence. The I-TNN with core matrix decomposition helps extract the weak debond defect information. The proposed approach is compared with general and state-of-the-art optical pulse thermography-based NDT algorithms. The experiment is carried out with two different

CFRP specimens with a flat and irregular shape having multiple debond defects with multiple depths and diameters. The results reflect the efficacy of the proposed algorithm in detecting the weak and noisy defect information from the irregular shape CFRP specimen with less computation time where other algorithms fail.

The rest of the paper is organized as; Section 2 presents the related work; Section 3 presents the proposed algorithm. Section 4 gives information about the experiment setup and specimen. Section 5 presents results and discussion. Section 6 concludes the paper.

II. RELATED WORK

The algorithms used for the debond detection in CFRP using optical thermography can be classified as post-processing techniques that are used to enhance the defect contrast and resolution and to remove the unwanted background noise from the thermal sequences. The debonds are the subsurface defects with varying depths and diameters that are difficult to detect by using only optical thermography due to uneven heating and thermal noise present in the thermal video sequences. To remove this thermal noise such that the defects are visible in the thermal sequences, post-image processing techniques are used. However, by using these techniques the debond defects with small depth and larger diameters are easily detected, but the debond defects with higher depth and smaller diameter are still a challenge. Further, if these debonds are on irregular shape specimens such as elbows and joints, the debond detection problem becomes much more severe. Some of the recent methods and techniques to cater to this problem are discussed below.

In [15], the authors proposed a new excitation method based on the laser thermal excitation for the debonding defect detection in the concrete specimen reinforced by fiber plastics. The authors validate their approach by providing numerical results and feasibility studies. In [16], the authors proposed a deep learning-based thermal image segmentation approach to quantify the debond defects in CFRP using optical thermography. The authors present a temporal and spatial deep network by integrating the cross-network learning strategy. The probability of detection is carried out as a quantitative measure in comparison with other algorithms and experiment results are presented for different CFRPs with debond defects. In [17], the authors present the wavelet feature-based thermal image segmentation for detecting debond defects in the CFRP using optical thermography. The PCA-based features are extracted from the thermal images which are further processed using the Gaussian Low Pass filtering in the wavelet domain. The F-score based comparison is presented with other recent algorithms. In [18], the authors propose a sparse low-rank matrix decomposition method for debond detection in CFRP. A joint decomposition is proposed with iterative sparse modeling. The visual results along with F-score based results are presented to prove the efficacy of the proposed model. In [19], the authors present a comparative study of extracting subsurface defects in thermal patterns. The non-negative matrix factorization methods are used and compared on the thermal data and results are presented in terms of detection accuracies. In [20], the authors present a comparison of tensor-based defect detection using the eddy current thermography. The importance of using tensor-based algorithms is highlighted. Further matrix and tensor decomposition-based algorithms are also compared. In [21], the authors propose a method of defect depth estimation in a CFRP specimen with flat bottom holes using pulsed thermography. The analysis is presented to characterize the defect depth with regard to specimen thickness and defect size. In [22], the authors propose an automated defect detection method in thermal sequences using important frame selection, feature extraction, and image segmentation to detect the defect size. In [23], the authors propose a Levenberg-Marquardt algorithm to remove the uneven heating noise in thermal sequences. A comparison is also presented with the existing algorithms in terms of noise removal and image resolution. In [24], the authors propose an image segmentation algorithm using artificial intelligence and fuzzy clustering for defect detection in thermal sequences. Experimental analysis is carried out to show the efficacy of the proposed model.

III. PROPOSED METHODOLOGY

First, given the thermographic video sequences $\mathcal{X} \in \mathfrak{R}^{n_1 \times n_2 \times n_3}$, where (n_1, n_2) are the spatial resolution and n_3 is the frame number. In tensor-based terminology, this is a three-way tensor [11], [12]. We propose a multilayer joint decomposition structure [9], [10] of low-rank (L) and sparse components (C) as;

$$\mathcal{X}^1 = \mathcal{L}^1 + \mathcal{C}^1 \tag{1}$$

For the second layer;

$$\mathcal{X}^2 = \mathcal{L}^2 + \mathcal{C}^2 + f^1(\mathcal{X}^1) \tag{2}$$

For the nth layer;

$$\mathcal{X}^n = \mathcal{L}^n + \mathcal{C}^n + f^{n-1}(\mathcal{X}^{n-1}) \tag{3}$$

where $f^n(X^n)$ is the activation used for the multilayer data modeling. To extract the defect information we propose the following optimization problem [11], [12];

$$\min_{\mathcal{L},\mathcal{C}} \|\mathcal{L}^n\|_* + \partial\|\mathcal{C}^n\|_1 \ s.t \ \mathcal{X}^n = \mathcal{L}^n + \mathcal{C}^n \tag{4}$$

where $\|.\|_*$ represents the tensor nuclear norm, ∂ is the regularizing parameter and $\|.\|_1$ is the l_1 norm. The problem in (4) is solved in the concatenated feature space using two steps. In the first step, the low-rank term is solved in the other step the sparse term is solved. Given the thermographic sequences and initializations a concatenated Eigen matrix decomposition is proposed as;

$$Y^n = \begin{bmatrix} X^n \\ X^n - C^{n-1} \\ C^{n-1} \end{bmatrix} \tag{5}$$

Where n is the layer number $X = \beta(\mathcal{X})$ is the tensor to matrix transformation and $\mathcal{X} = \beta^{-1}(X)$ is matrix to tensor transformation, same is used for $C \ and \ \mathcal{C}$. By joint concatenation of the low-rank and the sparse data, two benefits are obtained. First, we retain the original features of the thermographic sequences which helps prevent the estimated low-rank features to deviate from the original. Further, the residual data and sparse data allow us to embed the sparse

component into low-rank modeling which significantly helps to extract the weak defect information. It should be noted here, that this concatenation firstly occurs in the matrix feature space and the low-rank and sparse modeling is solved in the tensor feature space. This tensor-matrix sparse low-rank decomposition enables us to utilize both tools simultaneously. The problem in (5) is solved using a simple eigendecomposition as;

$$Y^n = U\Gamma V^T \tag{6}$$

Where U and V are the left and right Eigen matrices and Γ is the diagonal matrix containing the eigenvalues. The first six principal components are selected after the decomposition. Based on the repeated experimental analysis the first six components contain the most useful low-rank information namely.

Here $svt_{\partial_1}(\bar{S})$ is the singular value thresholding for the matrix, $sth(\mathcal{Y})$ is the soft thresholding for tensor [11] and $t - svt_{\frac{2}{\rho}}(\bar{L})$ represents the tensor singular value thresholding for the tensor [12]. For the parameters we set $\partial_1 = \frac{1}{\sqrt{n_{max}}}$, $n_{max} = \max(\min(n_1, n_2), n_3)$. Here (n_1, n_2, n_3) are the frames and rows and columns of core tensor respectively. $\partial = \frac{1}{\sqrt{\max(n_1, n_2)n_3}}$, $\rho = 1.1$ and the stopping condition is set as; $\|\mathcal{L}_{k+1} - \mathcal{L}_k\| \le \varepsilon$, $\varepsilon = 1e - 5$ based on our experimental analysis. For other applications, the parameters can be tuned accordingly.

$$\mathcal{Y}^n = \beta^{-1}((U\Gamma V^T)_{1 \text{ to } 6}) \tag{7}$$

A. Improved TNN with Core Tensor Decomposition

Let $\mathcal{A} = \mathcal{U} * \mathcal{S} * \mathcal{V}^*$ be the tensor singular decomposition (t-svd) of $\mathcal{A} \in \Re^{n_1 \times n_2 \times n_3}$. The tensor nuclear norm of $\mathcal{A}$ is given as [12];

$$\|\mathcal{A}\|_* := < \mathcal{S}, \mathcal{I} > = \sum_{i=1}^{r} \mathcal{S}(i, i, 1) \tag{8}$$

Where $r = rank_t(\mathcal{A})$ is the tensor tubal rank, $\mathcal{S}, \mathcal{I}$ is the singular value and identity tensor. To utilize the information in the third mode of the tensor svd we use the core singular matrix decomposition. The related operators are $\bar{S} = \beta(\mathcal{S})$ and $\mathcal{S} = \beta^{-1}(\bar{S})$, where β and β^{-1} are the transforms between the core tensor $\mathcal{S} \in \Re^{n_1 \times n_2 \times n_3}$ and core matrix $\bar{S} \in \Re^{n \times n_3}$, where $n = \min(n_1, n_2)$.

Further, the most significant components of this core tensor are found by approximating very few significant singular values. The core singular matrix approximation of the I-TNN rank is given as;

$$rank_i(\mathcal{A}) = [rank(\bar{S}), rank_t(\mathcal{A})]^T \tag{9}$$

Based on the above rank the I-TNN with core matrix approximation is given as;

$$\|\mathcal{A}\|_* = \|\bar{S}\|_* + \gamma \sum_{i=1}^{r} \mathcal{S}(i, i, 1) \tag{10}$$

Where γ is the balancing term. Based on the improved tensor nuclear norm and core matrix decomposition the problem in (4) can be solved iteratively using ADMM [13] for each layer.

$$\mathcal{L}_{k+1} = \arg\min_{\mathcal{L}} \|\mathcal{L}\|_* + \frac{\rho}{2} \left\| \mathcal{L} - \mathcal{Y} + \mathcal{C}_k - \frac{\mathcal{D}_k}{\rho} \right\|_F^2 \tag{11}$$

$$\mathcal{C}_{k+1} = \arg\min_{\mathcal{C}} \partial\|\mathcal{C}\|_1 + \frac{\rho}{2} \left\| \mathcal{L}_{k+1} - \mathcal{Y} + \mathcal{C} - \frac{\mathcal{D}_k}{\rho} \right\|_F^2 \tag{12}$$

$$\mathcal{D}_{k+1} = \mathcal{D}_k + \rho(\mathcal{Y} - \mathcal{L}_{k+1} - \mathcal{C}_{k+1}) \tag{13}$$

Where $\rho > 0$ is the augmented lagrangian penalty parameter, $\mathcal{D}$ is the dual variable, k is the iteration number. For the problem in (11), it is solved using ADMM [13] in two steps. The first step solves the core matrix problem and the other.

step solves the tensor nuclear norm problem. The optimization model for the two-step problem can be formulated as [11].

$$\bar{L}_{k+1} = \arg\min_{\beta(\mathcal{S})} \|\beta(\mathcal{S})\|_* + \frac{1}{2\partial_1} \left\| \mathcal{T} - \mathcal{Y} + \mathcal{C}_k - \frac{\mathcal{D}_k}{\rho} \right\|_F^2 \tag{14}$$

Where δ_1 is the regularizing parameter and $\mathcal{S}$ is from the t-svd and $\mathcal{T}$ is a temporary variable. The tensor with a low-rank core matrix can be given as;

$$\mathcal{Z}_{k+1} = \mathcal{U} * \beta^{-1}(\bar{L}_{k+1}) * \mathcal{V}^T \tag{15}$$

The other step minimized the tensor nuclear norm as follows;

$$\mathcal{L}_{k+1} = \arg\min_{\mathcal{L}} \|\mathcal{L}\|_* + \frac{\rho}{4} \|\mathcal{L} - \mathcal{Z}_{k+1}\|_F^2 \tag{16}$$

The details are given in the Table I.

TABLE I.   MULTILAYER ADMM FOR I-TNN WITH CORE MATRIX DECOMPOSITION

Input: Tensor data $\mathcal{X} \in \Re^{n_1 \times n_2 \times n_3}$

Initialization: Given $\rho, \partial_1, \partial, \mathcal{L} = 0, \mathcal{C} = 0, \mathcal{D} = 0$

For each layer n solve;

1. Solve the concatenated problem in (5) by (7) to get $\mathcal{Y}$
2. While not converged do:
3. Compute $[\mathcal{U}, \mathcal{S}, \mathcal{V}] = t - svd(\mathcal{Y} - \mathcal{C} + \frac{\mathcal{D}}{\rho})$
4. Update $\bar{S} := \beta(\mathcal{S})$
5. Compute $\bar{L} := svt_{\partial_1}(\bar{S})$
6. Update $\mathcal{Z} := \beta^{-1}(\bar{L})$
7. Update $\bar{\mathcal{L}} := \mathcal{U} * \mathcal{Z} * \mathcal{V}^T$
8. Update $\mathcal{L} := t - svt_{\frac{2}{\rho}}(\bar{L})$
9. Compute $\mathcal{C} := sth_{\frac{\partial}{\rho}}(\mathcal{Y} - \mathcal{L} + \frac{\mathcal{D}}{\rho})$
10. Update $\mathcal{D} := \mathcal{D} + \rho(\mathcal{Y} - \mathcal{L} - \mathcal{C})$
11. End while

Output: $\mathcal{L}^n, \mathcal{C}^n, \mathcal{D}^n$

IV. EXPERIMENTAL SETUP AND SPECIMEN DETAILS

Regarding the experimental setup, the OPT system available at our lab can be seen in Fig. 1. In the OPT system, halogen lamps are used as an excitation source to induce heat into the specimen. A $ZY - B$ type excitation source is used at the back of the halogen lamps with model $ITECH - IT6726G$. This model supports an adjustable power source that can be

tuned up to $3kW$. In our experiments, we set the power of the excitation source to $2kW$. The experiments are conducted in the reflection mode configuration [14]. The $85cm$ distance is selected between the lamps and the specimen. To capture the thermographs of the sample an infrared camera is used model $A655sc$. The output resolution of the infrared camera is set to 640×480 per frame. The infrared camera used has a thermal sensitivity of $0.05°C$. Further, a sampling frequency of $50Hz$ is selected for our experiments.

To validate the proposed model, two different CFRP specimen is selected. The CFRP specimen was obtained from the Chengdu Aircraft Design Institute of the China Aviation Industry. The obtained specimen is similar to the ones used in the design and manufacturing of aircraft and related components. The first specimen has a rectangular shape and a flat surface. The second sample is like a V shape with joints and edges. Both the specimen have debonded defects created

by inducing the Teflon inserts at various depths and different diameters. The detailed information about the specimen shape and defects can be found in Table II.
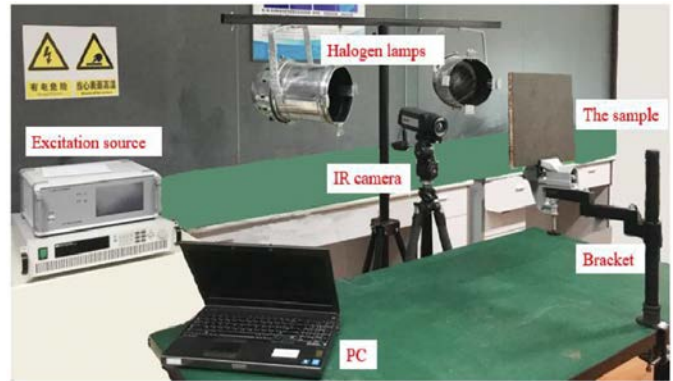

Fig. 1. The Optical Pulse Thermography System.

TABLE II. INFORMATION ABOUT THE CFRP SPECIMEN

Number	Defect Profile	Dimension(mm)	Defect Information(mm)	Picture
1		250×250×24.2	**Depth**:1, 2 **Diameter**:2,4,6,8,10,12,16, 20	
3		100×100×80	**Depth**:1.5,1.75,2,2.25,2.5,2 .75 **Diameter**:9, 10	

V. RESULTS AND DISCUSSION

In this section, the results are presented from the experiments. The visual results along with the F-score [9] and computation time are presented. The experiments are carried out using the optical pulse thermography system shown in Fig. 1. The repeated experiments were carried out to collect the thermographic sequences used. The reflection mode configuration is used with the standard camera, excitation source, and specimen distance given in [9]. The algorithms used in competition with the proposed algorithm are PPT [4], TSR [3], SPCT [6], EVBTF [9], and S-MoG [10]. The F-score and computation time results are given in Table III. The proposed algorithm was run up to four layers and the third layer results were found to be clear with better resolution and contrast for detecting the debond defects.

The defect detection results from the algorithms in comparison are given in a tabular form shown in Fig. 2. All the results for both specimens can be seen in Fig. 2. Fig. 2(Row 1) shows the comparative results for specimen 1. It is a rectangular-shaped specimen having a flat surface and 10 debond defects. The depths of the debonds are (1mm and 2mm) with varying diameter sizes. All the algorithms are run on a single computer to avoid any unfair processing advantage. From Fig. 2 (Row 1) it can be seen that most of the algorithms can detect at most 9 out of 10 defects. However, the strong noise is still present which limits the performance of algorithms in the scenario when the information about the defects is unknown. The proposed algorithm gives reasonable results with a reduction in noise and improvement in the resolution contrast of the specimen. The proposed algorithm can detect all defects where other algorithms fail.
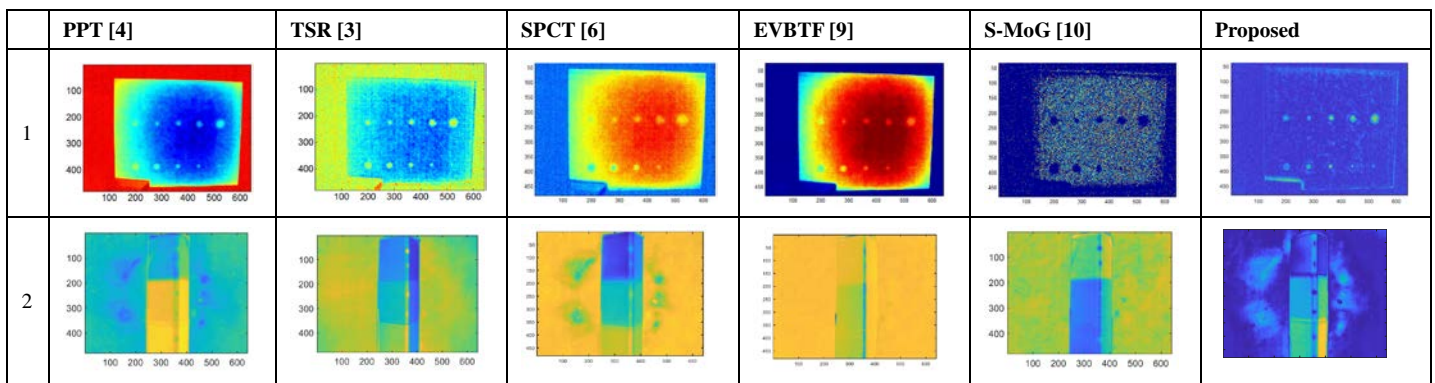
	PPT [4]	TSR [3]	SPCT [6]	EVBTF [9]	S-MoG [10]	Proposed
1						
2						

Fig. 2. The Comparative Analysis of different Algorithms.

TABLE III. COMPARATIVE RESULTS F-SCORE (LEFT) AND TIME TAKEN (RIGHT IN SECONDS)

Specimen Number	PPT [4]		TSR [3]		SPCT [6]		EVBTF [9]		S-MoG [10]		Proposed	
1	0.94	135	0.94	271	0.94	40	0.94	1342	0.94	173	**1**	**26**
2	0.75	146	0.88	601	0.88	43	0.75	753	0.88	125	**1**	**6**
Average	0.84	140	0.91	436	0.91	41	0.84	1046	0.91	149	**1**	**16**

Fig. 2(Row 2) shows the results for the second specimen. It has a V shape with an irregular surface. It is a more challenging specimen with defect depths ranging from $(1.5, 1.75, 2, 2.25, 2.5, 2.75)$mm. Here, the defect diameters are $(9 \text{ and } 10)$mm. It can be seen from Fig. 2(Row 2) that almost all algorithms fail to detect the debond defects. The strong noise is present and the resolution of the defects is quite poor. The proposed algorithm can detect all the defects with reasonable noise reduction and acceptable resolution. As the proposed algorithm utilizes a multilayer structure, the results in Fig. 2 are obtained by two layers of the algorithm. This layer number is selected based on the experimental analysis with multiple experiments on different data. However, due to the concatenated feature space where low-rank, sparse, and raw data are decomposed using a single feature space further layering does not significantly improve the results but in turn, incurs the additional computation cost. From the visual results, it can be argued that the proposed I-TNN with core matrix decomposition using a concatenated feature space in a multilayer architecture can detect smaller and deeper debond defects using OPT-NDT.

Table III shows the F-score and computation time results. For both specimens, the results are averaged in the last row of the Table III. On average, the PPT [4] and EVBTF [9] algorithms have the detection efficiency of 84% with 140sec and 1046sec as the average computation time. The TSR [3], SPCT [6] and S-MoG [10] algorithms have the 91 average percent of defect detection. Their running times are 436sec, 41 sec and 149sec respectively. The proposed model has 100% defect detection accuracy for the specimen under test. Using the concatenated feature space a simple eigen decomposition is carried out and only 6 principal eigen components are selected which help significantly in reducing the computation time enhancing the resolution of defects by multilayer I-TNN core matrix decomposition approach. The average computation time taken by the proposed model is 16sec.

VI. CONCLUSION AND FUTURE WORK

In this paper, a joint concatenation of the low-rank and sparse features is proposed. The I-TNN algorithm with core matrix-tensor decomposition in multilayer architecture is proposed for iteratively solving the feature space. The proposed approach is used for detecting the debond defects in the CFRP specimen using optical pulse thermography. By multi-layering, the low-rank and sparse components in a concatenated feature space help boost the convergence, eliminating the noise and detecting the debond defects with small diameter and varying depth. The comparative analysis with general OPT-NDT and other low-rank sparse and tensor modeling algorithms proves the debond detection capability of the proposed algorithm.

The possible future extensions of this work will be the testing of this work on several new and different CFRP specimens. Further, the proposed algorithm can be tested and validated on the eddy current thermography data, microwave thermography data, and other thermography data. Further apart from the debond detection the algorithm can also be used for other defects using as delaminations and crack in CFRP and other metal structures.

REFERENCES

[1] S. Marinetti et al., "Statistical analysis of IR thermographic sequences by PCA," Infrared Phys. Technol., vol. 46, no. 1–2, pp. 85–91, 2004.

[2] A. Hyvärinen and E. Oja, "Independent component analysis: algorithms and applications," Neural networks, vol. 13, no. 4–5, pp. 411–430, 2000.

[3] S. M. Shepard and M. F. Beemer, "Advances in thermographic signal reconstruction," in Thermosense: Thermal Infrared Applications XXXVII, 2015, vol. 9485, pp. 1–7.

[4] X. Maldague and S. Marinetti, "Pulse phase infrared thermography," J. Appl. Phys., vol. 79, no. 5, pp. 2694–2698, 1996.

[5] C. Ibarra-Castanedo and X. Maldague, "Pulsed phase thermography reviewed," Quant. Infrared Thermogr. J., vol. 1, no. 1, pp. 47–70, 2004.

[6] B. Yousefi, S. Sfarra, F. Sarasini, and X. P. V Maldague, "IRNDT inspection via sparse principal component thermography," in 2018 IEEE Canadian Conference on Electrical & Computer Engineering (CCECE), 2018, pp. 1–4.

[7] J.-Y. Wu, S. Sfarra, and Y. Yao, "Sparse principal component thermography for subsurface defect detection in composite products," IEEE Trans. Ind. Informatics, vol. 14, no. 12, pp. 5594–5600, 2018.

[8] L. Zhang, Q. Zhang, L. Zhang, D. Tao, X. Huang, and B. Du, "Ensemble manifold regularized sparse low-rank approximation for multiview feature embedding," Pattern Recognit., vol. 48, no. 10, pp. 3102–3112, 2015.

[9] P. Lu, B. Gao, Q. Feng, Y. Yang, W. L. Woo, and G. Y. Tian, "Ensemble variational Bayes tensor factorization for super resolution of CFRP debond detection," Infrared Phys. Technol., vol. 85, pp. 335–346, 2017.

[10] J. Ahmed, B. Gao, G. Y. Tian, Y. Yang, and Y. C. Fan, "Sparse ensemble matrix factorization for debond detection in CFRP composites using optical thermography," Infrared Phys. Technol., vol. 92, pp. 392–401, 2018.

[11] Y. Liu, L. Chen, and C. Zhu, "Improved Robust Tensor Principal Component Analysis via Low-Rank Core Matrix," IEEE J. Sel. Top. Signal Process., vol. 12, no. 6, pp. 1378–1389, 2018.

[12] C. Lu, J. Feng, W. Liu, Z. Lin, and S. Yan, "Tensor robust principal component analysis with a new tensor nuclear norm," IEEE Trans. Pattern Anal. Mach. Intell., 2019.

[13] R. Liu, Z. Lin, and Z. Su, "Linearized alternating direction method with parallel splitting and adaptive penalty for separable convex programs in machine learning," in Asian Conference on Machine Learning, 2013, pp. 116–132.

[14] Y. He, R. Yang, H. Zhang, D. Zhou, and G. Wang, "Volume or inside heating thermography using electromagnetic excitation for advanced composite materials," Int. J. Therm. Sci., vol. 111, pp. 41–49, 2017.

[15] Y. Xu and H. Sohn, "Nondestructive debonding detection of fiber reinforced plastics strengthened structure based on infrared thermal imaging with laser thermal excitation," in Sensors and Smart Structures Technologies for Civil, Mechanical, and Aerospace Systems 2020, 2020, vol. 11379, p. 1137914.

[16] Q. Luo, B. Gao, W. L. Woo, and Y. Yang, "Temporal and spatial deep learning network for infrared thermal defect detection," NDT E Int., vol. 108, p. 102164, 2019.

[17] J. Ahmed, G. A. Baloch, and G. Y. Tian, "Wavelet Domain Based Defect Detection using Optical Thermography," in ACM International Conference Proceeding Series, 2019, pp. 1–5, doi: 10.1145/3332340.3332356.

[18] J. Ahmed, B. Gao, W. L. Woo, and Y. Zhu, "Ensemble Joint Sparse Low-Rank Matrix Decomposition for Thermography Diagnosis System," IEEE Trans. Ind. Electron., vol. 68, no. 3, pp. 2648–2658, 2020.

[19] B. Yousefi, C. I. Castanedo, and X. P. V Maldague, "Measuring heterogeneous thermal patterns in infrared-based diagnostic systems using sparse low-rank matrix approximation: Comparative study," IEEE Trans. Instrum. Meas., vol. 70, pp. 1–9, 2020.

[20] Y. Liang, L. Bai, J. Shao, and Y. Cheng, "Application of Tensor Decomposition Methods In Eddy Current Pulsed Thermography Sequences Processing," in 2020 International Conference on Sensing, Measurement & Data Analytics in the era of Artificial Intelligence (ICSMD), 2020, pp. 401–406.

[21] Y. Wei, S. Zhang, Y. Luo, L. Ding, and D. Zhang, "Accurate depth determination of defects in composite materials using pulsed thermography," Compos. Struct., vol. 267, p. 113846, 2021.

[22] L. Yuan, X. Zhu, Q. Sun, H. Liu, P. Yuen, and Y. Liu, "Automatic extraction of material defect size by infrared image sequence," Appl. Sci., vol. 10, no. 22, p. 8248, 2020.

[23] D. Wang, Z. Wang, J. Zhu, and F. Ciampa, "Enhanced pre-processing of thermal data in long pulse thermography using the Levenberg-Marquardt algorithm," Infrared Phys. Technol., vol. 99, pp. 158–166, 2019.

[24] Z. Wang, L. Wan, N. Xiong, J. Zhu, and F. Ciampa, "Variational level set and fuzzy clustering for enhanced thermal image segmentation and damage assessment," NDT E Int., vol. 118, p. 102396, 2021.